

# Photonic Microwave Signal Processing Based on Opto-VLSI Technology

Feng Xiao<sup>1</sup>, Kamal Alameh<sup>1,2</sup> and Yong Tak Lee<sup>2,3</sup>  
*<sup>1</sup>Electron Science Research Institute, Edith Cowan University,  
<sup>2</sup>Department of Nanobio Materials and Electronics,  
Gwangju Institute of Science and Technology,  
<sup>3</sup>Department of Information and Communications,  
Gwangju Institute of Science and Technology,  
<sup>1</sup>Australia  
<sup>2,3</sup>Korea*

## 1. Introduction

The processing of radio frequency (RF) and microwave signals in the optical domain is an attractive approach to overcome the bottlenecks of bandwidth, power loss, and electromagnetic interference (EMI) encountered in conventional electronic signal processing systems. A wide range of emerging RF signal processing applications require specifically high resolution, ultra-wide bandwidth, wide-range tunability, and fast reconfigurability. While these requirements are difficult to achieve using conventional all-electronic processing, they are feasible with photonics-based signal processing.

Holography is an historic technology that allows the light scattered from an object to be recorded and reconstructed so that the object can reappear when a reference optical beam illuminates a hologram used to record that object. Holography has a wide range of applications such as optical signal storage and retrieval and information processing. The application of reconfigurable phase holograms to realize optical beam steering is an attractive field for either optical engineering or fundamental research. The reconfigurable phase holograms are calculated from the targeted beam steering pattern and implemented using spatial light modulator. Opto-VLSI processors are one of these devices that can dynamically generate phase holograms and perform optical beam steering.

Although full-electronic RF signal processing is very flexible and controllable, it is experiencing the bottlenecks of bandwidth and EMI. Processing microwave signals in the photonic domain can overcome the bottlenecks in the electronic signal processing. However the current technologies of microwave photonics have limited flexibility and reconfigurability. The Opto-VLSI technology is a novel and potential discipline that combine benefits of photonic devices and the intelligence plus processing capabilities of Very-Large-Scale Integrated (VLSI) circuits. It integrates intelligence into photonic systems providing a new foundation for a future information processing and communication systems and networks. This book chapter will discuss a new methodology of expanding the use of Opto-VLSI from the conventional paradigm of optical beam processing to a new frontier of

photonics-based RF signal processing, leading to a wide applications such as future broadband RF signal filters and beamformers for wireless systems for many wireless- and mobile-communication-related areas.

The application of holography in processing RF and microwave signals, which is implemented through an Opto-VLSI processor, offers many advantages over traditional microwave photonic methods in terms of flexibility and reconfigurability. The phase hologram is generated according to the applications of RF signal processing and uploaded onto the Opto-VLSI processor.

In this chapter, we discuss the use of holography for the applications of RF and microwave signal processing. This book chapter is organised as follows. In Section 2 a brief background on Opto-VLSI processors is provided. Section 3 discusses the use of holography to realize tunable microwave filters. In Section 4 the adaptive generation of true time delay (TTD) based on uploading appropriate phase hologram onto an Opto-VLSI processor is discussed. In Section 5 architecture of a tunable Opto-VLSI-based beamformer for phased array antennas is discussed. We conclude this chapter in Section 6.

## 2. Opto-VLSI processor

An Opto-VLSI processor is an array of liquid crystal (LC) cells driven by a Very-Large-Scale-Integrated (VLSI) circuit. Figure 1 shows a typical layout and a cell design of an 8-phase Opto-VLSI processor. It is driven by digital holographic diffraction gratings capable of steering/shaping incident optical beams as illustrated in Fig. 2. The voltage level of each pixel can individually be controlled by using a few memory elements that select a discrete voltage level and apply it, through the aluminium mirror electrode, across the LC cell. A transparent Indium-Tin Oxide (ITO) layer is used as the second electrode, and a quarter-wave-plate (QWP) layer is deposited between the LC and the aluminum mirror to accomplish polarization-insensitive operation. The ITO layer is generally grounded and a voltage is applied at the reflective electrode by the VLSI circuit below the LC layer. Opto-VLSI processors are electronically controlled, software-configured, polarization independent and are cost effective because of the high-volume manufacturing capability of VLSI chips as well as their capability of controlling multiple fiber ports in one compact Opto-VLSI module; they are also very reliable since beam steering is achieved with no mechanically moving parts.

By driving the Opto-VLSI with blazed gratings of different pitches, as shown in Fig. 3, optical beam steering can be achieved. The diffraction (or steering) angle for an Opto-VLSI processor,  $\alpha_m$ , is given by (Xiao *et al.*, 2008):

$$\alpha_m = \arcsin\left(\frac{m\lambda}{d}\right) \quad (1)$$

where  $m$  is the diffraction order (usually only the first order is considered),  $\lambda$  is the light wavelength in vacuum, and  $d$  is the grating period. By addressing each pixel independently a phase hologram can be synthesized leading to optical beam steering, beam shaping or multicasting. For example, a 4-phase Opto-VLSI processor having a pixel size of 5 microns can steer a 1550 nm laser beam by a maximum angle of around  $\pm 4^\circ$ . The maximum diffraction efficiency of an Opto-VLSI processor depends on the number of discrete phase levels that the VLSI can accommodate. The theoretical maximum diffraction efficiency is given by (Dammann, 1979):

$$\eta = \text{sinc}^2\left(\frac{\pi n}{M}\right) \tag{2}$$

where  $n = gM + 1$  is the diffraction order ( $n = 1$  is the desired order), and  $g$  is an integer. Thus an Opto-VLSI processor with binary phase levels can have a maximum diffraction efficiency of 40.5%, while a four phase level allow for efficiency up to 81%. The higher diffraction orders (which correspond to the cases  $g \neq 0$ ) are usually unwanted crosstalk signals, which must be attenuated or properly routed outside the output ports to maintain high signal-to-crosstalk performance.

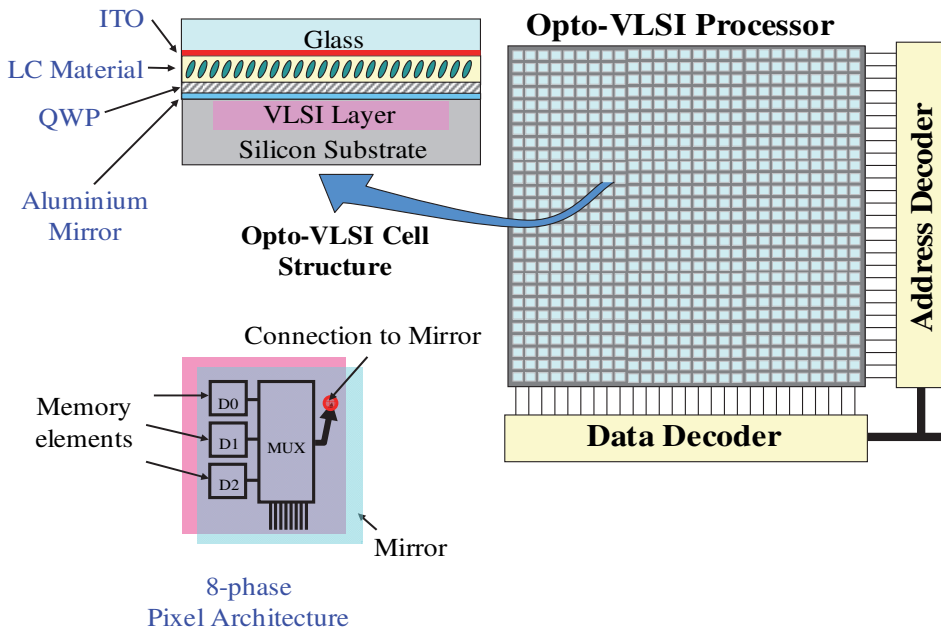


Fig. 1. Typical 8-phase Opto-VLSI processor and LC cell structure design.

Adaptive optical beam steering can be achieved by reconfiguring the phase hologram uploaded onto the Opto-VLSI processor. Recent advances in low-switching-voltage nematic LC materials and layer thickness control have allowed the incorporation of a thin quarter-wave-plate (QWP) layer between the LC and the aluminium mirror to accomplish polarization-insensitive multi-phase-level Opto-VLSI processors (Manolis *et al.*, 2002), as shown in Fig. 1. In addition, with current 130nm VLSI fabrication processes, VLSI chips featuring 24mm×24mm active area, maximum switching voltage of 3.0 volts, and pixel size of 5 microns, can be realised. Depositing low-switching-voltage electro-optic materials and QWP over such VLSI chips, can realize a polarization-insensitive Opto-VLSI processor that has a diffraction efficiency of 87% (0.6 dB loss) and a maximum steering angle of more than ±4.0°.

There have been different algorithms reported for the optimization of Opto-VLSI phase holograms to achieve effective beam steering, including simulated annealing and projection

methods. In our study, a modified simulated annealing method that can achieve accurate beam steering with low crosstalk is adopted (Yen-Wei Chen *et al.*, 2000).

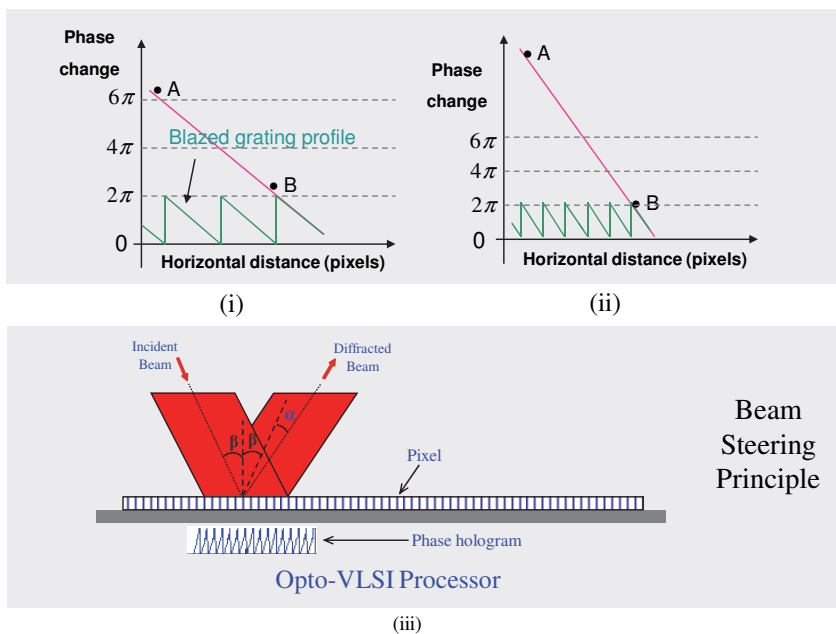


Fig. 2. Principle of beam steering through variable-pitch blazed grating generation.

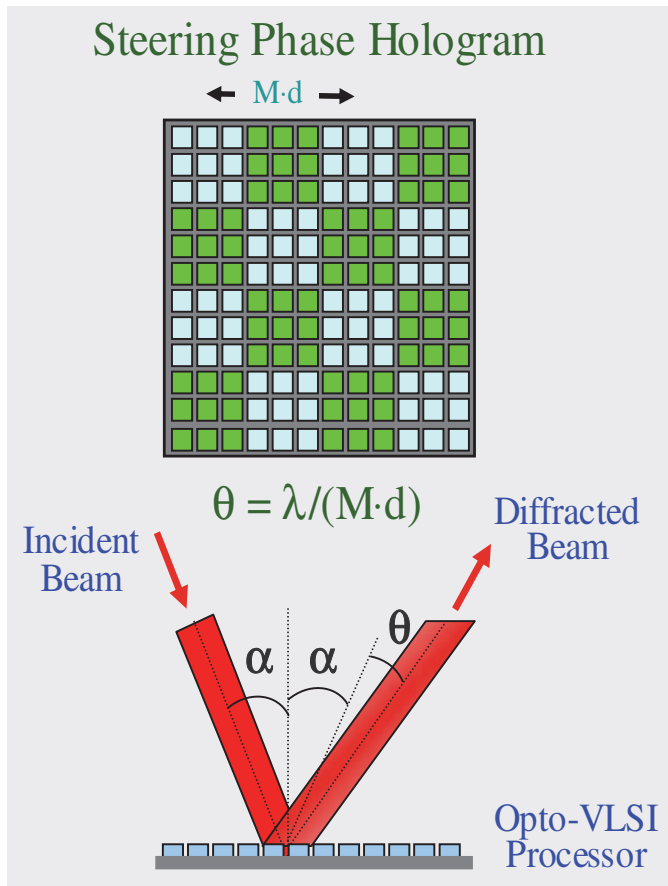


Fig. 3. Steering and multicasting capabilities of an Opto-VLSI processor.

### 3. Tunable photonic microwave filters

Photonics-based microwave and millimeter-wave filters offer advantages such as ultra-wide bandwidth, immunity to electromagnetic interference, and lightweight (Seeds&Williams, 2006; Capmany et al., 2006; Minasian, 2006). These advantages open new opportunities in a wide range of potential applications especially when high selectivity, resolution, wide tunability, and fast reconfigurability characteristics are required.

In recent years, numerous reconfigurable coherent-free photonic microwave transversal filter structures have been proposed and demonstrated, where multi-wavelength source is employed to suppress the optical interference in conjunction with modifying the optical tap weights or the time-delay increment between taps (Capmany et al., 1999; Polo et al., 2003; Ortigosa-Blanch et al., 2006; Hunter&Nguyen, 2006; Ning et al., 2007; Blals&Yao, 2008). Spectral slicing of an RF-modulated broadband optical source has been employed to generate different wavebands. However, the use of Bragg gratings or arrayed waveguide gratings for realizing spectral slicing results in fixed time-delay increments, which limit the

tunability of the photonic microwave transversal filter. Another approach to generating optical taps is the use of a tunable laser array, where each tunable laser element is dedicated to control the weight of a single optical tap. However, the main disadvantage of this approach is the high cost and reliability of the filter structure, especially when the number of taps increases.

As a powerful reconfigurable holography technology, a novel tunable photonic microwave filter has been proposed and experimentally demonstrated based on the use of an Opto-VLSI processor (Xiao et al., 2009). Through computer-generated phase holograms uploaded onto the Opto-VLSI processor, arbitrary spectral slicing with adaptive wavelength separations as well as independent tap weight control can be achieved. This demonstration has a significant advantage that the time-delay increment, tap numbers and tap weights can be adjusted independently and simultaneously, simply by electronics. This structure has the highest flexibility compared to previously reported microwave filter structures (Capmany et al., 2006; Zheng et al., 2006). The proposed tunable filter structure is a practical solution to realizing flexible and tunable microwave filters.

In Fig. 4, the proposed tunable photonic microwave filter is illustrated through an experimental setup. A broadband light source of amplified spontaneous emission (ASE) is externally modulated by an RF signal through an electro-optic modulator (EOM). The modulated light is amplified by an erbium doped fiber amplifier (EDFA) and routed via a circulator into a collimator which collimates the light into a 1-mm diameter beam. A 1200 line/mm grating plate disperses the incident beam into spectral components along different directions and linearly maps them onto the active window of an Opto-VLSI processor.

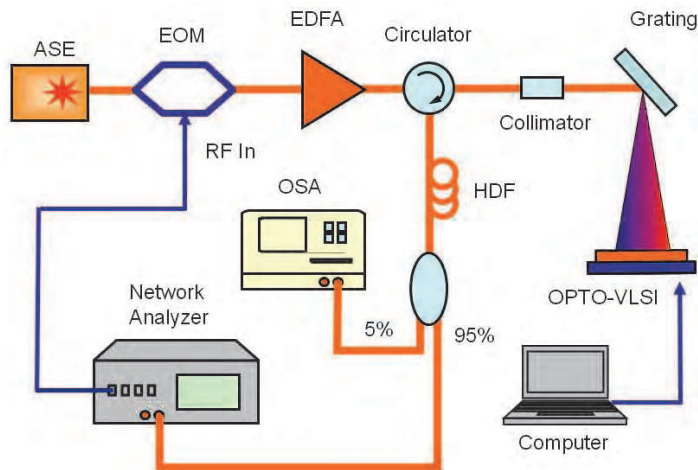


Fig. 4. Experimental setup for the tunable photonic microwave filter structure.

The wavelength of the optical field incident onto the Opto-VLSI processor varies along the pixels, which can be logically partitioned into pixel blocks by programming the Opto-VLSI processor. The spectral component, falling within the specific pixel block of the Opto-VLSI processor, can be either steered back along the incidence path thus coupling it back into the fiber collimator with minimum attenuation, or deliberately steered “off-track” so that its power is partially coupled back into the fiber collimator leading to an appropriate optical

attenuation for that spectral component. Therefore, by manipulating the phase hologram of individual pixel block, the power of each waveband component can be independently adjusted according to the required tap weights; and by partitioning the pixels into appropriate blocks, the optical taps with specific wavelength spacing can be picked out from the wideband light source while all the other wavebands are steered off-track and attenuated dramatically (Xiao *et al.*, 2008). For example, by applying an appropriate phase hologram consisting of 5 different blazed gratings, 5 different wavebands could be steered back and coupled to the collimator, as shown in Fig. 5. In other words, by configuring the phase hologram employed to the Opto-VLSI processor, tap weights and tap separations can be adjusted simultaneously, independently and continuously.

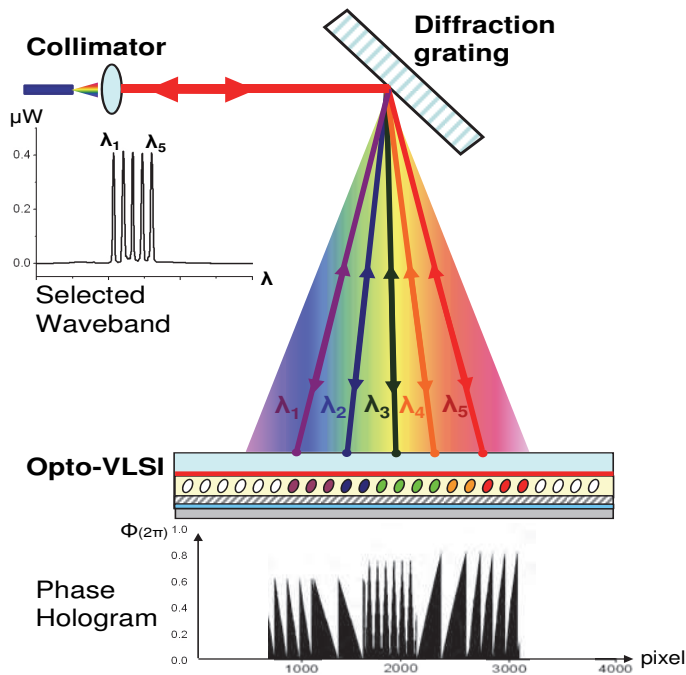


Fig. 5. The principle of optical waveband selection.

The optical taps that are coupled back into the fiber collimator are fed, through the circulator, to a high dispersion optical fiber, where the different RF-modulated wavebands experience different delay times. The delayed RF-modulated wavebands are finally photo-detected by a photo-receiver built into a Network Analyzer, which displays the microwave filter response. An optical spectrum analyzer (OSA) is also used as a monitor driven by a small fraction of the light detected by the photodiode of the Network Analyzer.

In the experiments, the RF signal generated by the Network Analyzer was used to intensity modulate the broadband ASE source using a JDS Uniphase electro-optical modulator of 4-GHz bandwidth. A 256-phase-level one-dimensional Opto-VLSI processor was used, which has  $1 \times 4096$  pixels, with  $1 \mu m$  pixel size and  $0.8 \mu m$  dead spacing between adjacent pixels. A Labview software was specifically developed to appropriately partition the pixel blocks so

that the optimum wavebands are selected. The pixel blocks are then driven by optimized phase holograms (blazed gratings) that steer the selected wavebands so that they are coupled back into the collimator. By optimizing the size and the phase profile of each pixel block, any desirable weight and time-delay increment is synthesized after the wavebands are launched into the high dispersion fiber (HDF), which has dispersion coefficient 382.5ps/nm and insertion loss 4.6 dB.

The response of the filter structure shown in Fig. 4 can be expressed as:

$$H(f) = \sum_{r=0}^M a_r \exp[-j2\pi r f \tau] \quad (3)$$

where  $f$  is the RF frequency,  $M$  is the number of the detected RF-modulated wavebands,  $a_r$  is the  $r^{\text{th}}$  tap weight, which is proportional to the optical power of the  $r$ th waveband, and  $\tau$  is the time delay between adjacent wavebands introduced by the high dispersion fiber. The time delay,  $\tau$ , can also be expressed in terms of the dispersion of the HDF as

$$\tau = \alpha \cdot \Delta\lambda \quad (4)$$

where  $\alpha$  denotes the dispersion coefficient of the HDF, and  $\Delta\lambda$  is the adjacent waveband separation.

The principle of the photonic microwave filter was demonstrated using 5 optical taps. Figures 6(a), 6(d), and 6(g) show the phase holograms applied to the Opto-VLSI processor to generate a constant time-delay increment with variable filter weights. The Opto-VLSI processor was partitioned into 5 pixel blocks corresponding to 5 wavebands, and the size of each pixel block was 400 pixels, resulting in a center-to-center waveband separation of 3.60 nm. For each pixel block, an optimum phase hologram was appropriately uploaded, so that the power level of the specific waveband was attenuated to an appropriate intensity. As shown in Figure 6(a), an appropriate phase hologram for each pixel block was employed to generate a normalized weight profile of [1, 1, 1, 1, 1]. Fig. 6(b) shows the selected wavebands measured by the OSA, and Fig. 6(c) shows the corresponding filter response. Note that the waveband coupled back into the collimator depends on the steering angle associated to this waveband and the numerical aperture of the collimator, and that the separation between adjacent wavebands depends on their pixel block sizes. The measured linewidth for each waveband was about 0.5 nm. Note that the spectral range illuminating each pixel block was around 3.6 nm. However, because this spectral range was diverging, only 0.5nm of this range was actually steered back and coupled into the collimator. By reconfiguring the phase holograms uploaded onto the various pixel blocks, the filter weights were varied to [0.4, 0.8, 1, 0.8, 0.4], and then to [0.2, 0.8, 1, 0.8, 0.2] as shown in Figs. 6(e) and 6(h). The corresponding filter responses are shown in Figures 6(f), and 6(i), respectively, where changes in rejection band and bandwidth are demonstrated, as a result of waveband attenuation.

Note that in Figures 6(c), 6(f) and 6(i) the solid lines denote the experimental results, which agree well with the simulation results calculated from Eq. (3,4), shown in dashed lines. All the filter responses shown in Fig. 6 exhibit a free-spectral range (FSR) of about 722 MHz and this is in good agreement with the specified dispersion coefficient of the HDF used in the experiments. The time delay increment, which is the product of the waveband separation and dispersion coefficient of the HDF, was 1.38 ns.

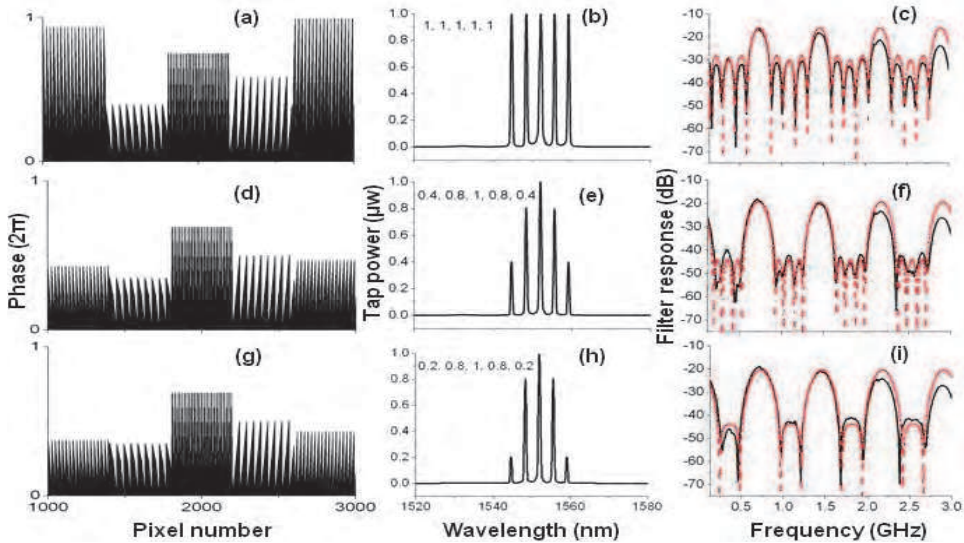


Fig. 6. Microwave filter tuning through tap weight control. (a), (d), and (g) phase hologram applied to the Opto-VLSI processor; (b), (e), and (h) selected RF-modulated wavebands; (c), (f), and (i) measured (solid line) and simulated (dashed line) filter responses for each case.

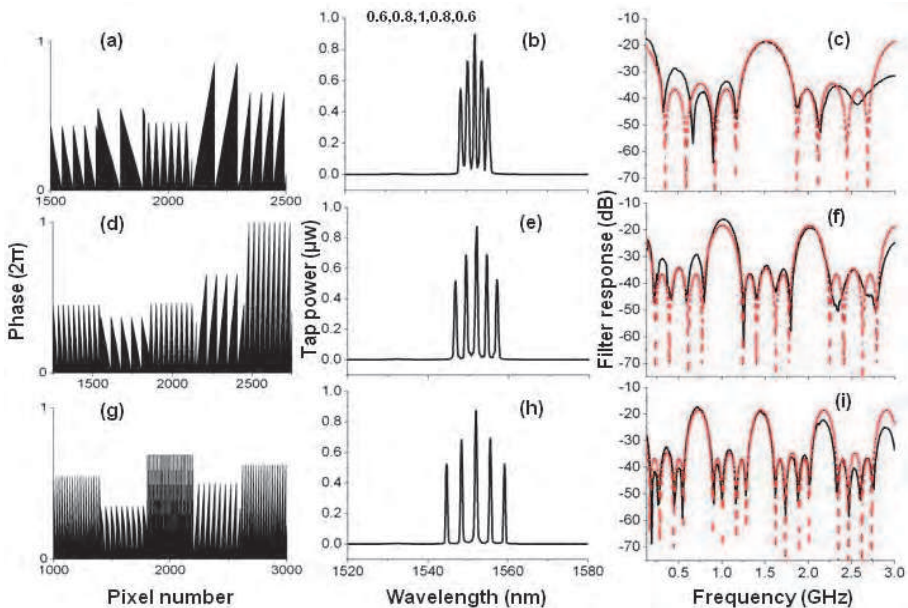


Fig. 7. Microwave filter tuning through time-delay increment control. (a,d,g) phase hologram applied to the Opto-VLSI processor; (b,e,h) selected RF-modulated wavebands; (c,f,i) measured (solid line) and simulated (dashed line) filter responses for each case.

The unique capability of the proposed tunable filter structure is its ability to continuously tune the time delay increment. This is accomplished by changing the spacing between adjacent pixel blocks (i.e., the pixel block size and center). Figures 7(a), 7(d), and 7(g) show the phase holograms applied to the Opto-VLSI processor to synthesize a normalized weight profile of [0.6, 0.8, 1.0, 0.8, 0.6] but different time delay increments. The corresponding wavebands are shown in Figures 7(b), 7(e), and 7(h). For these three cases, the sizes of the pixel blocks were 200, 300, and 400 pixels, respectively, corresponding to waveband separations of 1.72 nm, 2.60 nm, and 3.60 nm, respectively. Note that by optimizing the phase hologram for each pixel block, a normalized weight profile [0.6, 0.8, 1, 0.8, 0.6] was maintained in all cases. Figures 7(c), 7(f), and 7(i) show the corresponding measured (solid) and simulated (dashed) filter responses. It is evident from Fig. 7 that the tuning of the waveband separation (ie. the time delay increment) controls the free-spectral-range (FSR) as well as the bandwidth of the filter. For example, in Fig. 7, the FSR was reduced from 1.52 GHz, to 1.01 GHz, and then to 722MHz, and the filter bandwidth dropped from 216 MHz to 142 MHz and then to 86 MHz, when the time-delay increment was increased from 0.66 ns, to 0.99 ns, and then to 1.38 ns, respectively. Note that a good agreement between the simulated and measured filter responses is displayed in Fig. 7.

By investigating the filter responses shown in Figures 6(c, f, i) and Figures 7(c, f, i), one can see that the spectral response fades remarkably as the RF frequency increases. This is due to the interaction between the dispersion of the HDF and the nonzero optical bandwidth of each waveband (Taylor *et al.*, 2007; Pastor *et al.*, 2003a). This limitation is inherent to all filters that use spectral slicing. The bandwidth of the sliced wavebands in Fig. 6 and Fig. 7 was about 0.5 nm. Preliminary experimental results have shown that a narrower waveband bandwidth can be achieved using a higher dispersion grating plate and/or a larger distance between the grating and the Opto-VLSI processor.

Even though the optical tap generation involves fiber to free-space and free-space to fiber coupling, standard passive micro-assembly can be used to realise low-cost, robust and stable alignment without the need of automated high-precision stages (Baxter, 2006). Note that the maximum number of optical taps that can be generated depends on the bandwidth of the ASE source, the size of the active window of the Opto-VLSI processor, and the waveband separation. For our current experimental system, which based on the 1-D Opto-VLSI processor, up to 12 optical taps with the waveband separation of 2.60 nm can be generated. Note that, by using a 2-D Opto-VLSI processor, one can increase the number of optical taps significantly.

#### 4. Photonic true-time delay

Many current applications, such as RF imaging systems and wireless communications, are required to exhibit improved resolution, wider angular scans, and wide bandwidths. To obtain an optimal radiation pattern for broadband transmission, the signals received by or transmitted from the antenna array must be accurately time-compensated via true-time RF delay generation (Meijerink *et al.*, 2010; Jiang *et al.*, 2005). Currently electronic phase shift for phased-array antenna features the advantages of flexibility and reconfigurability. However, they are limited in their processing speed and bandwidth. In addition, the electronic phase shift control is accomplished through metallic coaxial cables or waveguide feeds which are heavy, bulky, lossy, and susceptible to electromagnetic interference (EMI) and crosstalk. The technology of digital signal processor (DSP) is currently thwarted either by the limited

resolution and the narrow bandwidth of analogue-to-digital converter, or by high power consumption of broadband analogue-to-digital converter.

The processing of radio frequency (RF) and microwave signals in the optical domain is an attractive approach to overcome the bottlenecks encountered in conventional electronic signal processing systems (Capmany *et al.*, 2005). A wide range of emerging RF signal processing applications require specifically high resolution, wide-range tunability, and fast reconfigurability. These requirements are difficult to achieve using conventional all-electronic processing, but feasible with photonics-based signal processing.

The use of photonics-based true time delay units has extensively been investigated in the last decade for applications ranging from modern microwave radar to wireless communication systems. In particular, broadband microwave phased-array antennas require the generation of variable true-time delays at each antenna element to realize beam or null steering, and optical fibers have been the best candidates for true-time delay synthesis. Compared with all-electrical techniques, optical true-time delay generation offers the advantages of broader bandwidth, lower insertion loss, higher phase stability, smaller size, lighter weight, and excellent immunity to both electromagnetic interference and crosstalk (Frigyes&Seeds, 1995; Italia *et al.*, 2005b; Y. Chen&Chen, 2002; Rideout *et al.*, 2007). Several approaches have been adopted to realise tunable true-time delay units, including the use of in-fiber chirped Bragg gratings (FBGs) (Italia *et al.*, 2005b), white cells or fiber delay lines in conjunction with MEMS (Mital *et al.*, 2006b; Anderson *et al.*, 2006; Vidal *et al.*, 2006), integrated optical waveguides (C. M. Chen *et al.*, 2010), optically-switched fiber delay structures (Tong&Wu, 1998), dispersion-enhanced photonic-crystal fibers (Jiang *et al.*, 2005), and higher-order mode dispersive multi-mode fibers (Raz *et al.*, 2004). However, most of these reported true-time delay architectures have mainly been used for realising beam steering in phased array antennas, and therefore, they do not have the flexibility to simultaneously generate multiple arbitrary true-time delays. In addition, such architectures can only generate discrete true-time delays, making them impractical for broadband null steering (Zmuda *et al.*, 2000). Zmuda *et al.* have reported a few adaptive true-time delay architectures based on the use of multiple tunable lasers in conjunction with high-dispersion fibres for the implementation of broadband nulling in microwave phased arrays (Zmuda *et al.*, 2000; Zmuda *et al.*, 1998). However, the use of multiple tunable lasers requiring continuous calibration makes the system implementation very expensive and impractical.

Recently, a novel true-time delay unit has been demonstrated through uploading appropriate holograms onto an Opto-VLSI processor to synthesize multiple arbitrary time delays (Juswardy *et al.*, 2009). This true-time-delay unit, which consists of a broadband optical source using Amplified Spontaneous Emission (ASE) and high dispersion fibers, has the capability to generate multiple true-time delays for several antenna elements simultaneously, making it attractive for broadband null-steering in phased array antennas.

The principle of the phased-array antenna architecture shown in Fig. 8 is demonstrated using the experimental setup illustrated in Fig. 4. In this setup, a broadband ASE source was modulated, via a JDS Uniphase electro-optical modulator (EOM) with a half-wave voltage of 6 V, by an RF signal which was generated using a 20 GHz network analyzer. The RF-modulated optical signal was amplified by an EDFA and collimated at 1-mm diameter and then launched onto a diffractive grating plate. The latter demultiplexed the collimated ASE beam into multiple RF-modulated wavebands, which were then mapped onto the active window of a 256-phase-level 1×4096-pixel Opto-VLSI processor of 1- $\mu\text{m}$  pixel size and 0.8- $\mu\text{m}$  dead spacing between adjacent pixels.

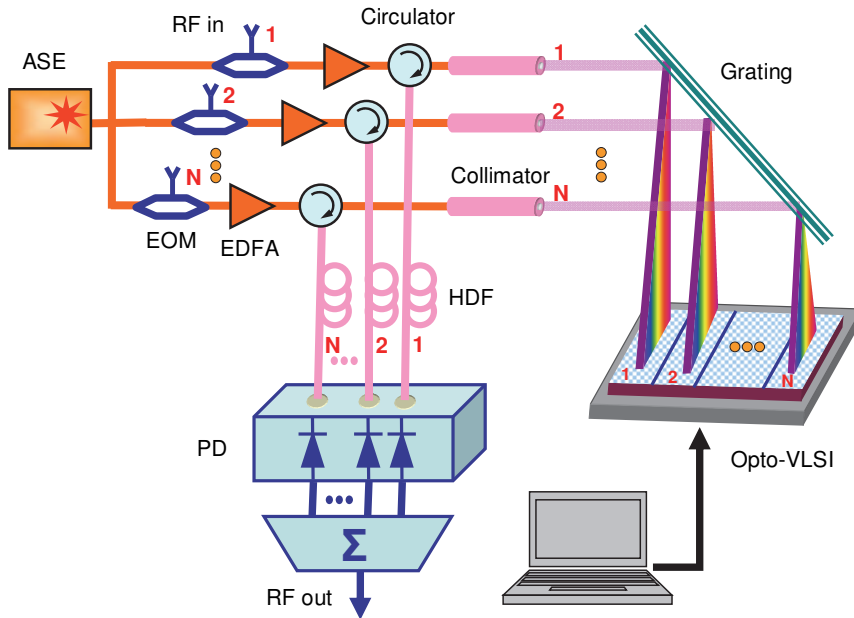


Fig. 8. Experimental setup used to demonstrate tunable time delay generation.

Labview software was specially developed to generate optimised phase holograms that couple the specific RF-modulated wavebands back into the fiber collimator, and at the same time equalize their intensities by changing the maximum phase levels applied to the different pixel blocks. The selected wavebands were then routed via a circulator to a 22-km high dispersion fiber (HDF) of dispersion coefficient 382.5 ps/nm and insertion loss 4.6 dB. An optical spectrum analyzer (OSA) was used to monitor the spectrum detected by a photodiode built in the Network Analyzer, as illustrated in Fig. 4.

One of the attractive features of the Opto-VLSI-based tunable time delay architecture is its ability to generate multiple RF delays without the need for RF splitters. Furthermore, the amplitude weight of each generated RF delay sample can simultaneously be controlled. This architecture offers excellent flexibility in applications such as phased-array null steering because multiple true-time RF delays for each antenna element can simultaneously be synthesized using computer generated holograms.

In order to measure the true-time-delay between the wavebands, the network analyzer was set to measure the RF response produced after the photodetection of the delayed RF-modulated wavebands. The transfer function that results from detecting  $M$  wavebands can be described as (Capmany et al., 2005):

$$H(f) = \sum_{r=0}^M a_r \exp[-j2\pi r f \tau] \quad (5)$$

Where  $f$  is the RF frequency,  $M$  is the number of the detected RF-modulated wavebands,  $a_r$  is the  $r$ th tap weight, which is proportional to the optical power of the  $r$ th waveband, and  $\tau$  is the time delay between adjacent wavebands introduced by the high dispersion fiber. The

free spectral range of the transfer function is given by the following equation (Capmany et al., 2005):

$$f_{FSR} = \frac{1}{\tau} \quad (6)$$

The time delay,  $\tau$ , can also be expressed in terms of the dispersion of the HDF as

$$\tau = \alpha \cdot \Delta\lambda \quad (7)$$

where  $\alpha$  denotes the dispersion coefficient of the HDF, and  $\Delta\lambda$  is the wavelength separation between the centers of two adjacent wavebands.

Note that, from Eq. 7, the time delay,  $\tau$ , depends on the dispersion coefficient of the dispersion medium, therefore, a higher dispersion medium results in a longer maximum attainable time delay.

The RF insertion losses of the whole tunable true-time delay system, defined as the RF power ratio between input and output of the RF signal, can be approximately expressed as (Capmany et al., 2006)

$$T_{RF} = \frac{P_{RFout}}{P_{RFin}} = \left( \frac{\pi P_{opt} T_{opt} Z_0}{2V_{\pi}} R \right)^2 \quad (8)$$

Where  $Z_0$  is the effective EOM RF input impedance or resistance of the EOM electrode,  $V_{\pi}$  is the voltage for a  $\pi$ -radian optical phase shift,  $R$  (A/W) is the photodetector responsivity,  $P_{opt}$  is the input continuous wave (CW) optical power to the EOM, and  $T_{opt}$  is the optical power transmission parameter that embraces all the optical losses and/or gain in the optical processing including the EOM insertion losses. In this experiment, the RF insertion loss is mainly due to the free-space optical system including the fibre collimator, the diffraction grating and the Opto-VLSI processor, which contributes around 12.5dB loss. Furthermore, the high dispersion fibre (HDF) and the EOM have insertion loss 4.6dB and 3.8dB, respectively. The total optical insertion loss of the entire system is around 21dB, whereas the EDFA provides a low gain of about 10dB due to saturation. The overall RF insertion loss in the experiment was about 25dB. However, this RF insertion loss can be compensated for by the use of an optical amplifier of 12.5dB gain placed after the HDF (before photodetection).

Different phase holograms, which are depicted in Fig. 9(a), were applied to the Opto-VLSI processor to generate five equally-separated RF-modulated optical wavebands with different wavelength separations as shown in Fig. 9(b). Fig. 9(c) shows the measured RF responses for seven true-time delay generation scenarios, corresponding to wavelength separations of 1.74nm, 2.64nm, 3.66nm, 4.32nm, 5.16nm, 5.88nm and 6.84nm, respectively.

The measured free spectral ranges of the various RF responses shown in Fig. 9(c) were used to calculate the true time delays, using Eq. 6. In addition, the measured waveband spacings (Fig. 9(b)) were also used to calculate the time delays for each scenario using Eq. 7. Table 1 summarizes the free spectral ranges of the various measured RF responses, the measured waveband separations, and their corresponding time delays calculated using Eq. 6 and Eq. 7, for the different scenarios. Excellent agreement between the true-time delays calculated using Eq. 6 and Eq. 7 is displayed in Table 1.

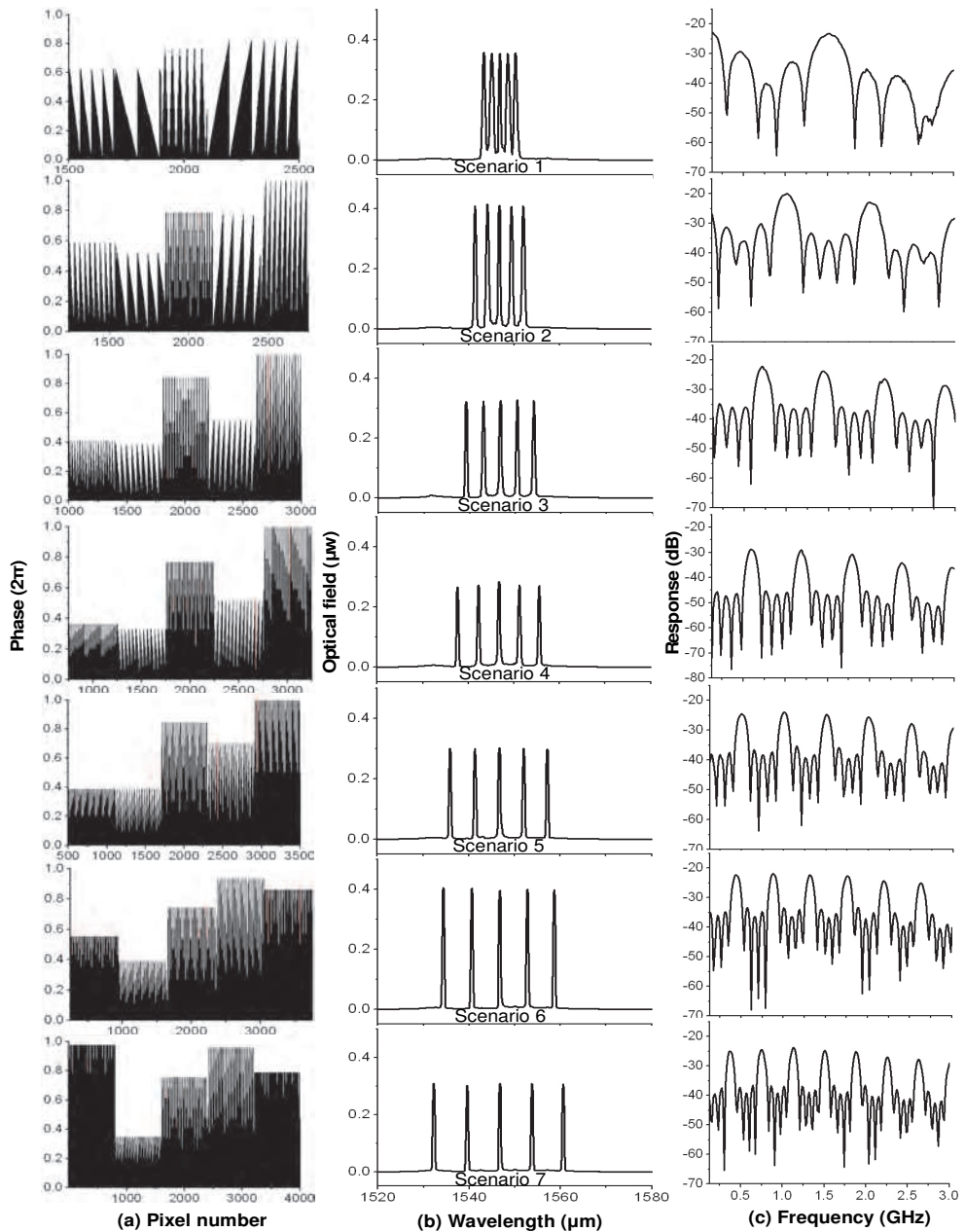


Fig. 9. (a) Opto-VLSI hologram, (b) Optical spectrum of 5 RF-modulated wavebands, (c) Measured RF responses due to the photodetection of the RF-modulated wavebands displayed in (b).

Note that the spectral response fades as the RF frequency increases, as shown in Fig. 9(c). This is due to the interaction between the dispersion of the HDF and the nonzero optical bandwidth of each waveband (Taylor *et al.*, 2007; Pastor *et al.*, 2003b). The bandwidth of the sliced wavebands in Fig. 9(b) was about 0.5 nm, and this caused about 4dB spectral walk-off at 3GHz. This limits the practical bandwidth of the proposed true-time delay system. However if the sliced wavebands are narrow, the walk off effect becomes insignificant as reported in (Pastor *et al.*, 2003b). In addition, our preliminary experimental results have shown that a narrower waveband can be achieved using a higher dispersion grating plate and/or a larger distance between the grating and the Opto-VLSI processor.

Note that the number of multiple time delays that can be generated simultaneously depend on (i) the spectral width of the ASE source, (ii) the maximum delay time (i.e., the maximum wavebands separation), and (iii) the size of the active window of the Opto-VLSI processor. The larger the size of the active window of the Opto-VLSI processor, the larger the number of time delays that can be generated. On the other hand, the more wavebands are required (more nulls), the smaller the maximum waveband separation that could be achieved, thus limiting the null angle which can be synthesized. Note, however, that for a certain number of nulls, the required number of wavebands for each antenna element is fixed. In this case the ASE source should have sufficient spectral width to ensure the synthesis of arbitrary null angles.

Finally, the experimental results shown in Fig. 9 and Table 1 confirm the ability of the Opto-VLSI-based true time delay unit to adaptively generate arbitrary RF delays for broadband null steering of phased array antennas. In order to generate multiple RF true-time delays for each antenna element, the Opto-VLSI processor was driven by optimised phase holograms that select and couple appropriate RF-modulated wavebands into a HDF that simultaneously delays the selected wavebands. To measure the generated time delays simultaneously, the selected wavebands were detected by a single photodetector to generate a microwave transversal filter response whose FSR and shape factor (measured by the network analyzer) can be used to calculate the amplitudes and delay times of the wavebands.

	Scenario 1	Scenario 2	Scenario 3	Scenario 4	Scenario 5	Scenario 6	Scenario 7
Measured FSR (GHz)	1.51	0.98	0.72	0.60	0.50	0.43	0.39
Time delay (ns) calculated using Eq.6	0.66	1.02	1.39	1.67	2.00	2.32	2.58
Measured waveband separation (nm)	1.74	2.64	3.66	4.32	5.16	5.88	6.84
Time delay (ns) calculated using Eq.7	0.67	1.02	1.41	1.66	1.99	2.26	2.63

Table. 1. Measured free spectral ranges, waveband separations, and their corresponding time delays calculated by Eq. 6 and Eq. 7.

This experiment demonstrated that arbitrary single or multiple true-time delays could be synthesized by slicing an RF-modulated broadband optical source and routing arbitrary sliced wavebands, through upload a phase hologram onto an Opto-VLSI processor, to a high-dispersion fiber where they experience RF delays that depend on their centre wavelengths.

## 5. Opto-VLSI-based tunable beamformer for microwave phased-array antenna

The growing demand for broadband mobile telephone, Internet and multimedia services, combined with the limited radio frequency (RF) spectrum availability, will require a substantial increase in the channel capacity of wireless and mobile communication systems. However, in current wireless network systems, the base station has no information on the position of each mobile user and radiates the RF signal in all directions within a cell in order to provide radio coverage. This results in inefficient utilization of the radiated power during the transmission and causes interference to adjacent cells (co-channel) that use the same frequency. In addition, the antenna receiver detects signals from all directions including noise and interference signals, making the processing of the desired signals complicated, thus limiting the transmission speed and the number of users.

Phased array antennas are rapidly becoming the new frontier of wireless communications because of their ability to overcome user-interference effects effectively and increase channel capacity substantially, together with a more efficient use of transmitted energy. Every phased array antenna requires a key element, “the beamformer”, which locates and tracks the various users associated to a base station and adapts the relative amplitude and phase shift at each antenna element so that the main lobe (highest gain) of the antenna is directed toward an active user, while nulls (i.e., where the directivity is zero) are adapted towards co-channel interferers. Phased array antennas refer to antenna arrays need adaptive signal processing capability to maximize the wanted signals and also minimize the interfering signals. Therefore, spatially-separated users can be served in the same base-station sector using the same frequency/time slot, which is called space division multiple access (SDMA) system.

The requirements for future phased array antenna beamformers include (i) the ability to perform wideband signal processing, (ii) short reaction time, (iii) small footprint (small size and light weight), (iv) increased coverage range and increased resolution, (v) reliability and maintainability, and (vi) low cost.

Currently, two beamforming approaches are mainly deployed in all-electronic phased array antennas. The first approach is based on the use of analogue RF phase shifters to adapt the antenna’s directivity pattern (Sorensen et al., 2004), while the second approach is based on digitising the antenna signals using analogue-to-digital converters and using digital signal processing (DSP) to control the mainlobe as well as the nulls of the antenna (Jian et al., 2008). Both analogue and digital beamforming approaches have the advantages of flexibility; however, both are inherently narrowband because of the limited instantaneous bandwidths of RF phase shifters and analogue-to-digital converters.

Photonics-based broadband phased-array antenna beamformers have been extensively investigated over the last decade for applications ranging from modern microwave radar to wireless communication systems. A broadband phased-array antenna requires the generation of variable true-time delays at each antenna element to realize beam or null steering. Several approaches have been adopted to realise tunable true-time delay units, including the use of in-

fibre chirped Bragg gratings (FBGs) (Italia *et al.*, 2005a), free-space in conjunction with white cells (Mital *et al.*, 2006a), integrated optical waveguides (Flamand *et al.*, 2000), optically-switched fibre delay structures (Tong&Wu, 1998). However, none of these reported photonics-based true-time delay units has the flexibility to either tune the true-time delay continuously or generate multiple tunable true-time delays for each antenna element simultaneously. Furthermore, the limited flexibility, reconfigurability, and tunability of current photonic beamformers make them impractical for realising broadband null steering.

Broadband null-steering beamformers are much more difficult to realise than beam-steering beamformers. Theoretical analysis of broadband null steering of phased-array antennas shows multiple variable true-time delays are needed for each antenna element, while only one variable true-time delay for an antenna element is required for broadband beam steering. An N-element smart antenna can synthesise (N-1) nulls only, and this requires the beamformer to simultaneously generate (2<sup>N-1</sup>-1) delayed versions of the RF signal received by the antenna.

Fig. 10(a) shows a typical N-element phased-array antenna architecture, whose array factor (or directional response) is given by (Zmuda *et al.*, 1998):

$$AF_N(\theta) = \prod_{n=1}^{N-1} (x - x_n) = \sum_{m=0}^{N-1} W_m x^m \tag{9}$$

where  $x = \exp[jkd \sin(\theta)]$ , d is the antenna element spacing, k = wave number =  $\omega/c$ , and  $x_n = x(\theta_n)$  is a zero of the polynomial  $AF_N$  corresponding to an antenna null at the angular coordinate  $\theta_n$ . Note that a change of even one zero affects all the weights,  $W_m$ . Note also that with N antenna elements, the phased-array antenna can synthesise only (N-1) nulls, as evident from Equation (9).

Without loss of generality, considering a 4-element phased array antenna, with its main lobe at an angle  $\theta$  and nulls located along angular coordinates,  $\theta_1$ ,  $\theta_2$ , and  $\theta_3$ , the array factor takes the form (Zmuda *et al.*, 2000):

$$AF_4(\theta) = \sum_{m=0}^3 W_m e^{jmkd \sin(\theta)} = (e^{jkd \sin(\theta)} - e^{jkd \sin(\theta_1)}) (e^{jkd \sin(\theta)} - e^{jkd \sin(\theta_2)}) (e^{jkd \sin(\theta)} - e^{jkd \sin(\theta_3)}) \tag{10}$$

By expanding Eq. (10), we obtain

$$AF_4(\theta) = x^3 - x^2 (e^{j\omega\tau_{21}} + e^{j\omega\tau_{22}} + e^{j\omega\tau_{23}}) + x (e^{j\omega\tau_{11}} + e^{j\omega\tau_{12}} + e^{j\omega\tau_{13}}) - e^{j\omega\tau_{01}} \tag{11}$$

From Eq. (11), it can be observed that for a 4-element phased array antennas, 2<sup>4-1</sup>-1 = 7 delay taps need to be generated by the true time delay unit in order to synthesis three nulls, and that the time delays required to be synthesized are:

$$\begin{aligned} \tau_{21} &= \frac{d}{c} \sin(\theta_1), \tau_{22} = \frac{d}{c} \sin(\theta_2), \tau_{23} = \frac{d}{c} \sin(\theta_3) \\ \tau_{11} &= \frac{d}{c} [\sin(\theta_1) + \sin(\theta_2)], \tau_{12} = \frac{d}{c} [\sin(\theta_1) + \sin(\theta_3)], \tau_{13} = \frac{d}{c} [\sin(\theta_2) + \sin(\theta_3)] \\ \tau_{01} &= \frac{d}{c} [\sin(\theta_1) + \sin(\theta_2) + \sin(\theta_3)] \end{aligned} \tag{12}$$

Generally, for an  $N$ -element broadband phased array, the synthesis of  $(N-1)$  broadband nulls can be achieved if the beamformer of the antenna can adaptively generate and combine  $(2^{N-1} - 1)$  delayed versions of the RF signals received by the antenna elements, as illustrated in Fig. 10(b).

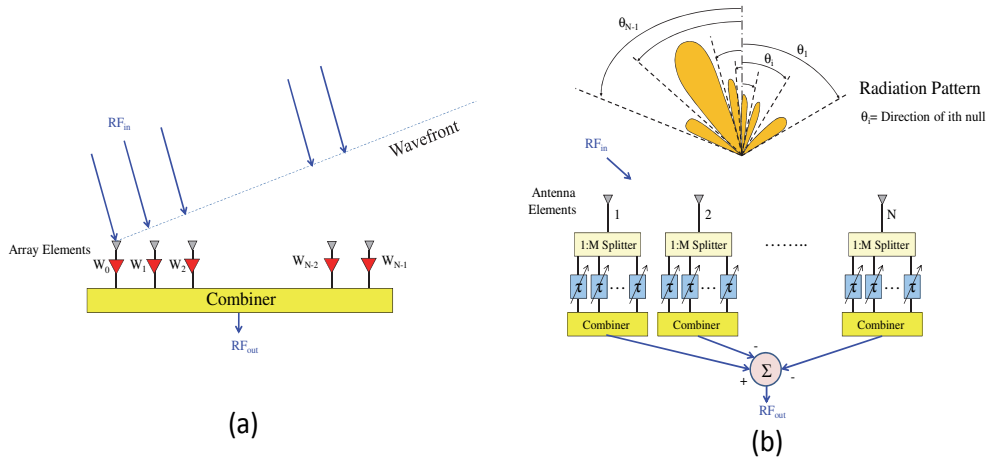


Fig. 10. (a) Typical phased-array antenna architecture. (b) Phased array antenna architecture for broadband null steering.

Recently a novel holographic-based broadband beamformer was proposed and demonstrated, employing an Opto-VLSI processor, a broadband light source, and high dispersion fibres to simultaneously generate arbitrary multiple true-time delays for each antenna element. This beamformer enables the realisation of adaptive multi-element antennas that significantly increase the capacity of next-generation wireless systems. The proposed beamformer has a number of novel features. First, it can adaptively achieve broadband beam- and null-steering through software; second, it incorporates microelectronics and photonics (Opto-VLSI) for RF signal processing, thus adding the flexibility, tunability, accuracy, and reconfigurability of microelectronics to the broadband capability of photonics; and third, it provides a cost-effective and compressed-hardware solution to multi-element antenna beamforming in next-generation wireless systems.

Figure 11 shows the proposed Opto-VLSI-based RF phased-array antennas architecture as well as experimental setup for synthesis of broadband beam steering. The structure was set to tune four fiber lasers, all controlled by a single 2-D Opto-VLSI processor with 8-bit phase level,  $512 \times 512$  pixels of a pixel size of  $15\mu\text{m}$ . Each tunable fiber laser employed an Erbium-doped fiber amplifier (EDFA) operating in C-band, an optical coupler, a polarization controller (PC), and a circulator. The broadband amplified spontaneous emission (ASE) noise resulting from the optical amplifier was split by the optical coupler with a 5/95 power splitting ratio, where 5% of ASE power was used to extract the output of the tunable fiber laser while the remaining 95% was re-circulated in the fiber ring cavity to generate lasing. The polarization controller was used to optimize the diffraction efficiency of the grating plate and to enforce single-polarization lasing. All broadband ASE signals directed to the corresponding collimator array ports via optical circulators were collimated at about 0.5 mm

diameter. An optical lens (Lens 1) with 10 cm focal length was used between the collimator array and a diffraction grating plate to focus the collimated ASE beams onto a small spot onto the grating plate. The grating plate, having 1200 lines/mm and a blazed angle of  $70^\circ$  at 1530 nm, spatially de-multiplexed the ASE beams, and spread the ASE spectra into different directions. Another optical lens (Lens 2) with the same focal length, located in the middle position between the grating plate and the Opto-VLSI processor, was used to collimate the dispersed optical beams and map them onto the surface of the 2-D Opto-VLSI processor, which was partitioned into 4 rectangular pixel blocks by software. Each pixel block was assigned to a tunable laser and used to efficiently couple back any part of the ASE spectrum illuminating this pixel block along the incident path into the corresponding collimator port. The Opto-VLSI processor can arbitrarily select any wavebands that are mapped onto its surface using the principle of beam steering described above. The selected wavebands were coupled back into the corresponding fiber collimator port, and then routed back to the gain medium via the corresponding circulator, thus forming an optical loop for single-mode laser generation.

A Labview software was developed to generate and upload the optimized digital phase holograms that simultaneously steer the desired wavebands for each channel and couple back into the corresponding collimators for subsequent recirculation in the fiber loops. Four different wavelengths can independently be selected for lasing within the different fiber loops by uploading appropriate phase holograms (blazed grating) that drive all the pixel blocks of the Opto-VLSI processor. Therefore, this structure enables generation of multiple tunable fiber laser sources, each of which can be independently tuned and output from a specific output port, which offers excellent flexibility to synthesis beam and null steering.

Each RF signal received by the element at the front-end of the phase-array antennas was used to intensity modulate the wavelength channels using an Electro-Optic Modulator (EOM). All the RF-modulated optical signals were coupled into a single fiber and routed into an EDFA for amplification, and then launched into a 10-km Corning LEAF non-zero dispersion shifted optical fiber with dispersion coefficient about 4.2 ps/nm/km and insertion loss of 0.2 dB/km at 1550 nm. Each RF-modulated optical signal experienced a true-time delay that depended on their centre wavelengths, before they were finally detected by a photo-diode that produced the sum of the delayed RF signals. In this way, the TTD between adjacent antenna elements were generated by controlling the wavelength spacing between the various wavelength channels. One of the attractive features of the proposed phased array antenna architecture shown in Fig. 1 is its ability to simultaneously generate all the tunable RF true-time delays for the smart antenna beamformer through optimised phase holograms uploaded onto the Opto-VLSI processor. Various phase holograms, which were synthesized and optimized for specific beam steering scenarios, were stored to enable beamsteering scenarios to be recalled through software.

Experiments were conducted using the setup illustrated in Fig. 11 to evaluate the performance of a 4-element rectangular patch type smart antenna system for flexible beam steering. The antenna elements were separated at a distance of 99 mm, corresponding to half of the RF operating wavelength thus alleviating the effect of side lobes. By refreshing phase holograms generated for the four pixel blocks, the lasing wavelengths can be tuned in terms of their wavelength separations needed to generate the TTD required for RF beam steering.

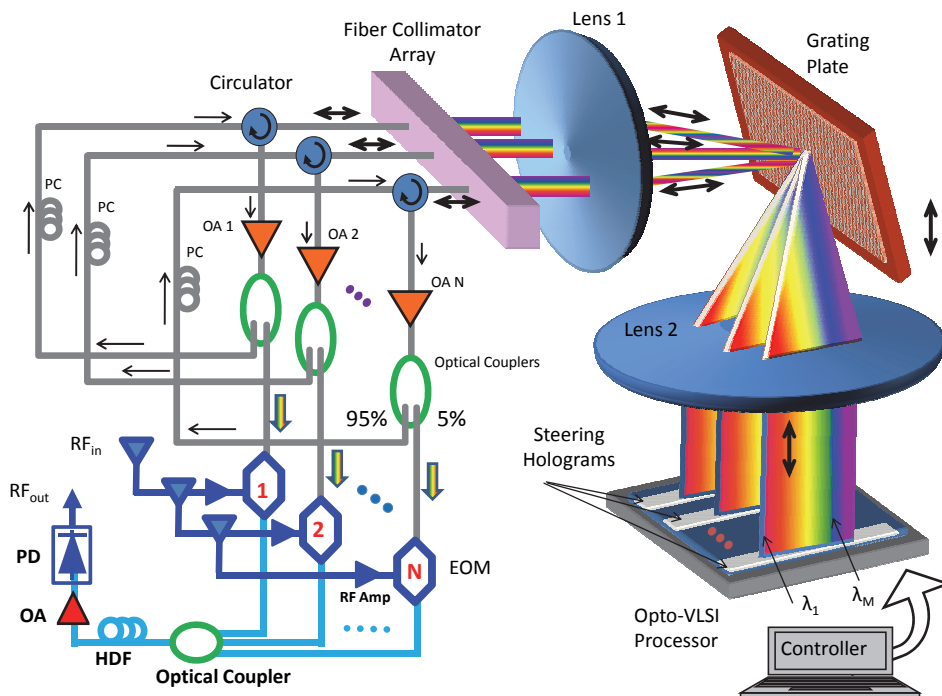


Fig. 11. Opto-VLSI-based phased array antenna architecture for broadband beam steering.

For each beamsteering scenario, the RF signal produced after the photodetection of the delayed RF-modulated optical signals was monitored by an RF power meter. Figures 12 (a-d) show several scenarios of measured antenna radiation patterns (right) corresponding to different equi-spaced wavelength channels (left) generated by the Opto-VLSI processor. For example, in Fig. 12 (a), the Opto-VLSI processor generated a wavelength spacing of 1 nm, which corresponds to 42-ps delay between adjacent antenna elements. The measured beamsteering angle was about  $7^\circ$ , which is in excellent agreement with the theoretical prediction of  $7.2^\circ$ . When the spacing between the laser channels was increased from 1 nm to 4 nm, the measured main lobe was steered from  $7^\circ$  to around  $30^\circ$ , as illustrated in Fig. 12. These experimental results agree very well with the theoretical predictions, demonstrating the excellent capability of the Opto-VLSI processor to realize a phased-array antenna beamformer.

Note that this structure has the capability of null steering if each laser channel is able to generate multiple laser wavelengths. Single or multiple arbitrary wavelengths for each laser channel can be generated and the amplitude of each laser of different wavelength can also be controlled simply by uploading the appropriate steering phase holograms onto the Opto-VLSI processor that can not only select arbitrary multiple wavelengths to lase but also control their cavity losses thus their output powers. Each pixel blocks steers a waveband along its initial path or slightly off-track so that variable optical attenuation (and hence RF attenuation) is achieved for all delayed RF signal simultaneously.

The experiments demonstrated an Opto-VLSI-based tunable beamformer for adaptively steering the radiation patter of RF phased array antennas. By using phase holograms implemented by a single Opto-VLSI processor 4 independent optical wavebands can be generated and their spectral tuned, leading to 4 independent tunable fiber lasers. The RF-modulated lasers are used to generate TTD in 4-element rectangular patch arrayed antennas. Experimental results show the capability of the proposed structure to perform RF beam steering between 0°-30°.

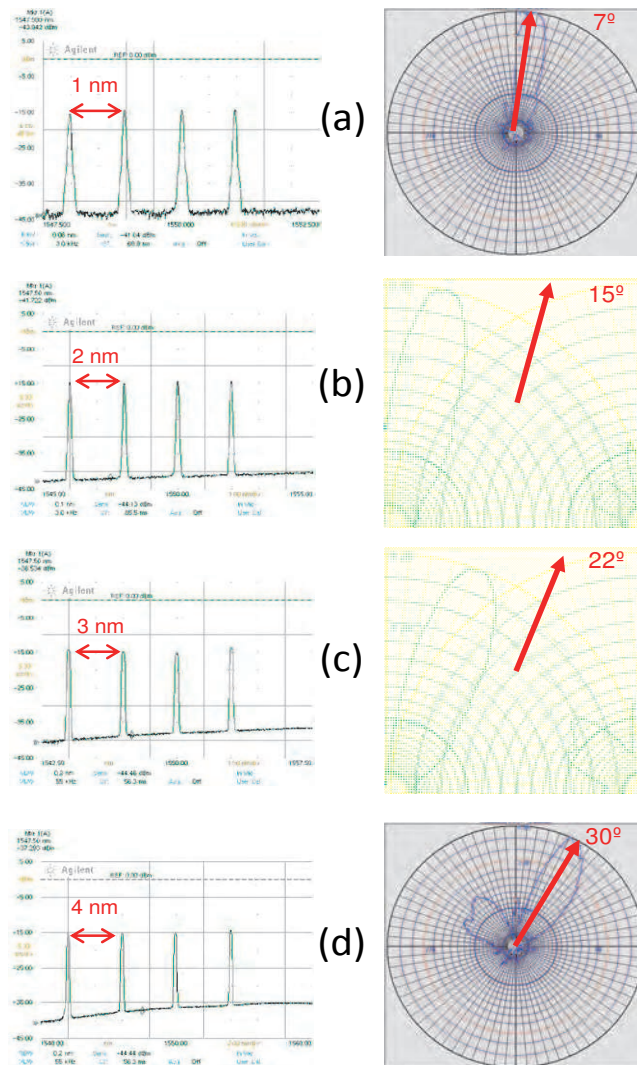


Fig. 12. Opto-VLSI-based tunable laser generations (left), and the corresponding RF beam steering profile measured in the experiments (right).

## 6. Conclusion

In this chapter, we discussed the reconfigurable phase holograms for the realization of microwave & RF filters, true-time delays, and beamformers, for the first time ever, to overcome the previous disadvantages of poor tunability, inflexibility, and low-resolution of conventional photonic microwave signal processors. By uploading appropriate phase holograms onto an Opto-VLSI processor, (i) full control for tap weights and tap spacings has been achieved to realize a reconfigurable RF filter; (ii) arbitrary single or multiple true-time delays could be synthesized; and (iii) a beamformer for 4-element phased-array antennas has been demonstrated. These work shows that holography is a promising technology to flexibly process microwave & RF signals with high resolution and wide waveband.

## 7. Acknowledgement

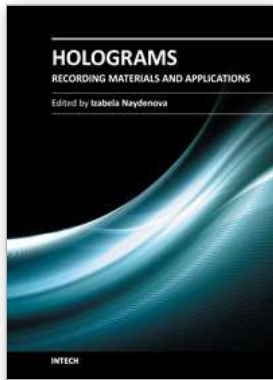
We acknowledge the support of the Department of Nano-bio Materials and Electronics, Gwangju Institute of Science and Technology, Republic of Korea, for the development of the Opto-VLSI processor.

## 8. References

- Anderson, B. L., Rabb, D. J., Warnky, C. M. & Abou-Galala, F. (2006). Binary Optical True-Time Delay Based on the White Cell: Design and Demonstration. *J. Lightwave Technol.*, Vol. 24, pp. 10
- Baxter, G. F., S.; Abakoumov, D.; Hao Zhou; Clarke, I.; Bartos, A.; Poole, S.; (2006). Highly programmable Wavelength Selective Switch based on Liquid Crystal on Silicon switching elements. In *Proc. OFC/NFOEC*, Vol. OTuF2Anaheim, California, USA: OSA.
- Blals, S. R. & Yao, J. P. (2008). Tunable photonic microwave filter using a superstructured FBG with two reflection bands having complementary chirps. *Ieee Photonics Technology Letters*, Vol. 20, pp. 199-201, Issn: 1041-1135.
- Capmany, J., Ortega, B. & Pastor, D. (2006). A tutorial on microwave photonic filters. *Journal of Lightwave Technology*, Vol. 24, No. 1, pp. 201-229, Issn: 0733-8724.
- Capmany, J., Ortega, B., Pastor, D. & Sales, S. (2005). Discrete-time optical processing of microwave signals. *Journal of Lightwave Technology*, Vol. 23, No. 2, pp. 702-723, Issn: 0733-8724.
- Capmany, J., Pastor, D. & Ortega, B. (1999). New and flexible fiber-optic delay-line filters using chirped Bragg gratings and laser arrays. *Ieee Transactions on Microwave Theory and Techniques*, Vol. 47, No. 7, pp. 1321-1326, Issn: 0018-9480.
- Chen, C. M., Yi, Y. J., Wang, F., Yan, Y. F., Sun, X. Q. & Zhang, D. M. (2010). Ultra-Long Compact Optical Polymeric Array Waveguide True-Time-Delay Line Devices. *Ieee Journal of Quantum Electronics*, Vol. 46, No. 5, pp. 754-761, Issn: 0018-9197.
- Chen, Y.-W., Yamauchi, S., Wang, N. & Nakao, Z. (2000). A fast kinoform optimization algorithm based on simulated annealing. *IEICE Trans. Fundamentals*, Vol. E83-A, No. 4, pp. 3
- Chen, Y. & Chen, R. T. (2002). A fully packaged true time delay module for a K-band phased array antenna system demonstration. *IEEE Photon. Technol. Lett.*, Vol. 14, pp. 3
- Dammann, H. (1979). Spectral characteristics of stepped-phase gratings. *Optik*, Vol. 53 pp. 9

- Feng Xiao, Budi Juswardy, and Kamal Alameh, "Tunable Photonic Microwave Filters Based on Opto-VLSI Processors" *IEEE Photonics Technology Letters*, vol. 21, pp. 751-753 (2009).
- Flamand, G., De Mesel, K., Moerman, I., Dhoedt, B., Hunziker, W., Kalmar, A., Baets, R., Van Daele, P. & Leeb, W. (2000). InP-based PIC for an optical phased-array antenna at 1.06  $\mu$  m. *Ieee Photonics Technology Letters*, Vol. 12, No. 7, pp. 876-878, Issn: 1041-1135.
- Frigyes, I. & Seeds, A. J. (1995). Optical generated true-time delay in phased array antennas. *IEEE Trans. Microw. Theory Tech.*, Vol. 43, pp. 9
- Hunter, D. B. & Nguyen, L. V. T. (2006). Widely tunable RF photonic filter using WDM and a multichannel chirped fiber grating. *Ieee Transactions on Microwave Theory and Techniques*, Vol. 54, No. 2, pp. 900-905, Issn: 0018-9480.
- Italia, V., Pisco, M., Campopiano, S., Cusano, A. & Cutolo, A. (2005a). Chirped fiber Bragg gratings for electrically tunable time delay lines. *Ieee Journal of Selected Topics in Quantum Electronics*, Vol. 11, No. 2, pp. 408-416, Issn: 1077-260X.
- Italia, V., Pisco, M., Campopiano, S., Cusano, A. & Cutolo, A. (2005b). Chirped Fiber Bragg Gratings for Electrically Tunable Time Delay Lines. *IEEE J. Sel. Top. Quantum Electron*, Vol. 11, pp. 9
- Jian, L., Huali, W. & Guanghui, X. (2008). GA-Based digital multi-beam reconfiguration for satellite phased array antennas. In *Microwave and Millimeter Wave Technology, 2008. ICMMT 2008. International Conference on*, 1164-1166.
- Jiang, Y. Q., Howley, B., Shi, Z., Zhou, Q. J., Chen, R. T., Chen, M. Y., Brost, G. & Lee, C. (2005). Dispersion-enhanced photonic crystal fiber array for a true time-delay structured X-band phased array antenna. *Ieee Photonics Technology Letters*, Vol. 17, No. 1, pp. 187-189, Issn: 1041-1135.
- Juswardy, B., Xiao, F. & Alameh, K. (2009). Opto-VLSI-based photonic true-time delay architecture for broadband adaptive nulling in phased array antennas. *Optics Express*, Vol. 17, No. 6, pp. 4773-4781, Issn: 1094-4087.
- Manolis, I. G., Wilkinson, T. D., Redmond, M. M. & Crossland, W. A. (2002). Reconfigurable multilevel phase holograms for Optical switches. *IEEE Photon. Technol. Lett.*, Vol. 14, No. 6, pp. 801-803
- Meijerink, A., Roeloffzen, C., Meijerink, R., Zhuang, L. M., Marpaung, D., Bentum, M. J., Burla, M., Verpoorte, J., Jorna, P., Hulzinga, A. & van Etten, W. (2010). Novel Ring Resonator-Based Integrated Photonic Beamformer for Broadband Phased Array Receive Antennas-Part I: Design and Performance Analysis. *Journal of Lightwave Technology*, Vol. 28, No. 1, pp. 3-18, Issn: 0733-8724.
- Minasian, R. A. (2006). Photonic signal processing of microwave signals. *Ieee Transactions on Microwave Theory and Techniques*, Vol. 54, No. 2, pp. 832-846, Issn: 0018-9480.
- Mital, R., Wamky, C. M. & Anderson, B. L. (2006a). Design and demonstration of an optical true-time-delay device based on an octic-style white cell. *Journal of Lightwave Technology*, Vol. 24, No. 2, pp. 982-990, Issn: 0733-8724.
- Mital, R., Warnky, C. M. & Anderson, B. L. (2006b). Design and Demonstration of an Optical True-Time-Delay Device Based on an Octic-Style White Cell. *J. Lightw. Technol.*, Vol. 24, pp. 9
- Ning, G., Shum, P. & Zhou, J. Q. (2007). Chromatic dispersion effect on microwave photonic filter with a tunable linearly chirped fiber bragg grating. *Microwave and Optical Technology Letters*, Vol. 49, No. 9, pp. 2131-2133, Issn: 0895-2477.

- Ortigosa-Blanch, A., Mora, J., Capmany, J., Ortega, B. & Pastor, D. (2006). Tunable radio-frequency photonic filter based on an actively mode-locked fiber laser. *Optics Letters*, Vol. 31, No. 6, pp. 709-711, Issn: 0146-9592.
- Pastor, D., Ortega, B., Capmany, J., Sales, S., Martinez, A. & Munoz, P. (2003a). Optical microwave filter based on spectral slicing by use of arrayed waveguide gratings. *Optics Letters*, Vol. 28, No. 19, pp. 1802-1804, Issn: 0146-9592.
- Pastor, D., Ortega, B., Capmany, J., Sales, S., Martinez, A. & Munoz, P. (2003b). Optical microwave filter based on spectral slicing by use of arrayed waveguide gratings. *Opt. Lett.*, Vol. 28, pp. 1802-1804
- Polo, V., Vidal, B., Corral, J. L. & Marti, J. (2003). Novel tunable photonic microwave filter based on laser arrays and  $N \times N$  AWG-based delay lines. *Ieee Photonics Technology Letters*, Vol. 15, No. 4, pp. 584-586, Issn: 1041-1135.
- Raz, O., Rotman, R., Danziger, Y. & Tur, M. (2004). Implementation of photonic true time delay using high-order-mode dispersion compensating fibers. *Ieee Photonics Technology Letters*, Vol. 16, No. 5, pp. 1367-1369, Issn: 1041-1135.
- Rideout, H. R., Seregelyi, J. S. & Yao, J. P. (2007). A true time delay beamforming system incorporating a wavelength tunable optical phase-lock loop. *Journal of Lightwave Technology*, Vol. 25, No. 7, pp. 1761-1770, Issn: 0733-8724.
- Seeds, A. J. & Williams, K. J. (2006). Microwave photonics. *Journal of Lightwave Technology*, Vol. 24, No. 12, pp. 4628-4641, Issn: 0733-8724.
- Sorensen, R. K., Iskander, M. F. & Lee, J. J. (2004). Low-cost nonplanar microstrip-line ferrite phase shifter utilizing circular polarization. *Ieee Microwave and Wireless Components Letters*, Vol. 14, No. 1, pp. 25-27, Issn: 1531-1309.
- Taylor, J. D., Chen, L. R. & Gu, X. J. (2007). Simple reconfigurable photonic microwave filter using an arrayed waveguide grating and fiber Bragg gratings. *Ieee Photonics Technology Letters*, Vol. 19, No. 5-8, pp. 510-512, Issn: 1041-1135.
- Tong, D. T. K. & Wu, M. C. (1998). Multiwavelength optically controlled phased-array antennas. *Ieee Transactions on Microwave Theory and Techniques*, Vol. 46, No. 1, pp. 108-115, Issn: 0018-9480.
- Vidal, B., Mengual, T., Ibanez-Lopez, C. & Marti, J. (2006). Optical beamforming network based on fiber-optical delay lines and spatial light modulators for large antenna arrays. *Ieee Photonics Technology Letters*, Vol. 18, No. 21-24, pp. 2590-2592, Issn: 1041-1135.
- Xiao, F., Juswardy, B., Alameh, K. & Lee, Y. T. (2008). Novel broadband reconfigurable optical add-drop multiplexer employing custom fiber arrays and Opto-VLSI processors. *Optics Express*, Vol. 16, No. 16, pp. 11703-11708, Issn: 1094-4087.
- Zheng, R., Alameh, K. E. & Wang, Z. L. (2006). A tunable photonic RF notch filter based on opto-VLSI technology. *Microwave and Optical Technology Letters*, Vol. 48, No. 6, pp. 1011-1015, Issn: 0895-2477.
- Zmuda, H., Toughlian, E. N., Jones, M. A. & Payson, P. M. (2000). Photonic architectures for broadband adaptive nulling with linear and conformal phased array antennas. *Fiber and Integrated Optics*, Vol. 19, No. 2, pp. 137-154, Issn: 0146-8030.
- Zmuda, H., Toughlian, E. N., Payson, P. & Klumpe, H. W. (1998). A photonic implementation of a wide-band nulling system for phased arrays. *Ieee Photonics Technology Letters*, Vol. 10, No. 5, pp. 725-727, Issn: 1041-1135.



## **Holograms - Recording Materials and Applications**

Edited by Dr Izabela Naydenova

ISBN 978-953-307-981-3

Hard cover, 382 pages

**Publisher** InTech

**Published online** 09, November, 2011

**Published in print edition** November, 2011

Holograms - Recording Materials and Applications covers recent advances in the development of a broad range of holographic recording materials including ionic liquids in photopolymerisable materials, azo-dye containing materials, porous glass and polymer composites, amorphous chalcogenide films, Norland optical adhesive as holographic recording material and organic photochromic materials. In depth analysis of collinear holographic data storage and polychromatic reconstruction for volume holographic memory are included. Novel holographic devices, as well as application of holograms in security and signal processing are covered. Each chapter provides a comprehensive introduction to a specific topic, with a survey of developments to date.

### **How to reference**

In order to correctly reference this scholarly work, feel free to copy and paste the following:

Feng Xiao, Kamal Alameh and Yong Tak Lee (2011). Photonic Microwave Signal Processing Based on Opto-VLSI Technology, Holograms - Recording Materials and Applications, Dr Izabela Naydenova (Ed.), ISBN: 978-953-307-981-3, InTech, Available from: <http://www.intechopen.com/books/holograms-recording-materials-and-applications/photonic-microwave-signal-processing-based-on-opto-vlsi-technology>

# **INTECH**

open science | open minds

### **InTech Europe**

University Campus STeP Ri  
Slavka Krautzeka 83/A  
51000 Rijeka, Croatia  
Phone: +385 (51) 770 447  
Fax: +385 (51) 686 166  
[www.intechopen.com](http://www.intechopen.com)

### **InTech China**

Unit 405, Office Block, Hotel Equatorial Shanghai  
No.65, Yan An Road (West), Shanghai, 200040, China  
中国上海市延安西路65号上海国际贵都大饭店办公楼405单元  
Phone: +86-21-62489820  
Fax: +86-21-62489821

© 2011 The Author(s). Licensee IntechOpen. This is an open access article distributed under the terms of the [Creative Commons Attribution 3.0 License](#), which permits unrestricted use, distribution, and reproduction in any medium, provided the original work is properly cited.